Statistical Atlases for Electroanatomical Mapping of Cardiac Arrhythmias

Mihaela Constantinescu[1], Su-Lin Lee[1], Sabine Ernst[2], and Guang-Zhong Yang[1]

[1] The Hamlyn Centre for Robotic Surgery, Imperial College London, London, UK
[2] The Royal Brompton and Harefield Hospital, London, UK
mihaela.constantinescu12@imperial.ac.uk

Abstract. Electroanatomical mapping is a mandatory time-consuming planning step in cardiac catheter ablation. In practice, interventional cardiologists target specific endocardial areas for mapping based on personal experience, general electrophysiology principles, and preoperative anatomical scans. Effective fusion of all available information towards a useful mapping strategy has not been standardised and achieving the optimal map within time and space constraints is challenging. In this paper, a novel framework for computing optimal endocardial mapping locations in patients with congenital heart disease (CHD) is proposed. The method is based on a statistical electroanatomical model (SEAM) which is instantiated from preoperative anatomy in order to achieve an initial prediction of the electrical map. Simultaneously, the anatomical areas with the highest frequency of mapping among the similar cases in the dataset are detected and a classifier is trained to filter these points based on the electroanatomical data. The framework was tested in an iterative process of adding mapping points to the SEAM and computing the instantiation error, with retrospective clinical data of 66 CHD cases available.

1 Introduction

Cardiac rhythm disorders are serious life-long comorbidities affecting patients with surgical repair of congenital heart disease (CHD). These life-threatening conditions are commonly treated by radiofrequency (RF) catheter ablation with a high input from the clinician in terms of personalised electroanatomical mapping, RF energy delivery and follow-up. CHD electroanatomical mapping is additionally challenging due to the structural differences in anatomy and unusual haemodynamics. All these physiological changes affect the electrical conduction system and build the substrate for arrhythmias uncommon to normal hearts, but specific to each CHD in particular [4].

Pre-procedural planning is a major factor in the success and duration of cardiac catheter ablation. The state-of-the-art in intra-operative image guidance systems such as CARTO (Biosense Webster, Diamond Bar, CA, USA) or EnSite (St Jude Medical, St Paul, MN, USA) are able to reconstruct the anatomy from the mapping catheter tip motion and the electrical activation from the

catheter tip electrode. However, the catheter tip can only be in contact with the endocardium at sparse points and while a large number of points yields better mapping accuracy, this increases pre-procedural time. Emerging multi-electrode systems such as Rhythmia (Boston Scientific, Marlborough, MA, USA with their basket catheter configuration limit the reachability of narrow sites in CHD patients, despite being able to collect many mapping points in the same time [6]. Moreover, the construction of a clinically informative map is a skill of experienced clinicians, who are able to adapt general electrophysiology principles to the specific CHD and patient anatomy and to decide on the position of the mapping points.

As part of the procedural pre-planning and also for better understanding of the electrophysiology, several electromechanical models have been proposed [10, 14]. The models were built and parameterised from a small number of measurements, thus limiting the instantiation ability at finer level of deformed anatomy and atypical activation caused for example by surgical scars. Other approaches focused on improving the electrophysiology model by coupling a generic equation of the anisotropic myocardial fibre orientation [7] and further enhancing it with ECG-derived measures [16]. However, these have proved unable to describe activation patterns measured intraoperatively [7].

Parameterisation of shape atlases has also been in extensive use in describing cardiac anatomy. Since their introduction [5], statistical shape models (SSM) have moved from simple shape descriptions on Riemannian manifolds to more complicated multi-dimensional spaces such as parameters of rigid transformations [3] and to combined statistical atlases of shape and texture [1] or shape and pose [11], thus showing their applicability outside the traditional point distribution models commonly implemented in cardiac shape analysis. Furthermore, combined inter- and intra-subject shape modelling has been used in the study of cardiac [9] and respiratory motion [15]. In CHD patients, shape analysis on the myocardium in Tetralogy of Fallot showed that disease-specific markers can be computed from medical images [8, 17]. Moreover, the values differed significantly from the healthy subjects, thus encouraging cohort-specific statistical analysis.

In this paper, a novel approach for optimal electroanatomical mapping of CHD is proposed. Firstly, a statistical electroanatomical model (SEAM) is built for each disease and cardiac chamber separately. Secondly, the frequency of anatomical sites chosen as mapping points in the specific CHD anatomy is computed. Finally, the vertices of a new shape are classified into mapping and regular points based on the atlas electroanatomical knowledge and sorted in descending order of their mapping frequency across the anatomy-specific dataset. The framework was tested in 5 CHD groups, adding to 66 CHD electrophysiology studies, to propose subject-specific mapping points location and compute the error reduction in electrical feature instantiation of the SEAM, i.e. unipolar and bipolar voltages and local activation times (LAT). The instantiation errors from the proposed sequence of mapping points were compared against the instantiation errors from the retrospective sequence of mapping points acquired in CARTO.

The results showed a steeper reduction in the electroanatomical reconstruction error when the mapping points were selected with the proposed approach.

2 Methods

2.1 Data Acquisition

Electroanatomical data from CARTO 3 studies of 66 CHD anatomies was exported. Two CHD groups were represented: Tetralogy of Fallot (34 studies) and univentricular hearts repaired by Fontan procedure with total cavo-pulmonary connection (32 studies). In the Fallot group, there were 21 studies of right ventricle (RV) and 13 of right atrium ($\mathrm{RA_{Fallot}}$), while in the Fontan group, there were 16 left atria (LA), 9 right atria ($\mathrm{RA_{Fontan}}$), and 7 total cavo-pulmonary connections (TCPC).

Each CARTO study included the preoperative MRI, the fast electroanatomical map (FAM) created by the mapping catheter, the unipolar and bipolar voltages and the LAT at each FAM vertex, the list and position of the sparse mapping points, as well as the rigid transformation from the intraoperative manual registration of the MRI onto the FAM. The number of mapping points varied within the same anatomy and the same CHD, with 49±35 points in RV, 35±18 in $\mathrm{RA_{Fallot}}$, 33±21 in LA, 34±23 in $\mathrm{RA_{Fontan}}$, and 33±22 in TCPC. The MRI meshes were smoothed in MeshLab [2].

For each of the five groups, an analysis inspired by mutual information was performed, in order to select as template the mesh that is closest to the group mean in terms of Cartesian distance and unipolar and bipolar voltages and LAT difference between pairwise vertices. This yielded 6206 vertices for RV, 3940 for $\mathrm{RA_{Fallot}}$, 6508 for LA, 7973 for $\mathrm{RA_{Fontan}}$, and 5086 for TCPC. The correspondences were chosen as the list of vertices on each template mesh and were propagated on the other meshes using landmark-free nonrigid registration [12]. In order to match the electrical values, the MRI meshes were registered nonrigidly on their corresponding FAM. All distances and electrical values were normalised within each case dataset.

2.2 Statistical Models

A statistical shape model was first built to fit a new shape $\mathbf{s}$ to the atlas described by the mean shape $\bar{\mathbf{s}}$ and the matrix of eigenvectors $\mathbf{P}_\mathrm{a}$. The shape $\mathbf{s}$ was approximated by the SSM as $\hat{\mathbf{s}}_\mathrm{a}$ from the set of parameters $\mathbf{b}_\mathrm{a}$, the result of least square optimisation. This can be represented by:

$$\hat{\mathbf{s}}_\mathrm{a} = \bar{\mathbf{s}} + \mathbf{P}_\mathrm{a}\mathbf{b}_\mathrm{a} \tag{1}$$

Simultaneously, the correspondences on shape $\mathbf{s}$ built a subset of an instance in the statistical electroanatomical model (SEAM) defined by the mean electroanatomical vector $[\bar{\mathbf{s}}^\mathrm{T}\ \bar{\mathbf{e}}^\mathrm{T}]^\mathrm{T}$ and the eigenvectors $\mathbf{P}_\mathrm{ae}$. Again using least square

optimisation, the current electroanatomical vector $[\mathbf{s}^{\mathrm{T}}\ \mathbf{e}^{\mathrm{T}}]^{\mathrm{T}}$ was approximated as $[\hat{\mathbf{s}}_{\mathrm{ae}}^{\mathrm{T}}\ \hat{\mathbf{e}}^{\mathrm{T}}]^{\mathrm{T}}$, defined by the model through the parameters $\mathbf{b}_{\mathrm{ae}}$ (Eq. (2)).

$$\begin{bmatrix}\hat{\mathbf{s}}_{\mathrm{ae}}\\ \hat{\mathbf{e}}\end{bmatrix} = \begin{bmatrix}\bar{\mathbf{s}}\\ \bar{\mathbf{e}}\end{bmatrix} + \mathbf{P}_{\mathrm{ae}}\mathbf{b}_{\mathrm{ae}} \tag{2}$$

Due to least square optimisation forcing the approximated shape to converge to the original in both models, it can be assumed that $\mathbf{s} \approx \hat{\mathbf{s}}_{\mathrm{a}} \approx \hat{\mathbf{s}}_{\mathrm{ae}}$ and therefore $\mathbf{P}_{\mathrm{a}}\ \mathbf{b}_{\mathrm{a}} \approx \mathbf{P}_{\mathrm{ae,s}}\mathbf{b}_{\mathrm{ae}}$, whereby $\mathbf{P}_{\mathrm{ae,s}}$ is the matrix formed by the rows of $\mathbf{P}_{\mathrm{ae}}$ corresponding to the shape vector $\mathbf{s}$. Finally, the unknown parameter vector $\mathbf{b}_{\mathrm{ae}}$ and subsequently the electrical values $\hat{\mathbf{e}}$ can be recovered as in Eq. (3) and (4), where $\mathbf{P}_{\mathrm{ae,s}}^{+} = (\mathbf{P}_{\mathrm{ae}}^{\mathrm{T}}\ \mathbf{P}_{\mathrm{ae}})^{-1} \cdot \mathbf{P}_{\mathrm{ae}}^{\mathrm{T}}$ is the Moore-Penrose pseudoinverse of $\mathbf{P}_{\mathrm{ae,s}}$ and $\mathbf{P}_{\mathrm{ae,e}}$ are the rows of matrix $\mathbf{P}_{\mathrm{ae}}$ corresponding to the electrical value vector.

$$\mathbf{b}_{\mathrm{ae}} \approx \mathbf{P}_{\mathrm{ae,s}}^{+}\mathbf{P}_{\mathrm{a}}\mathbf{b}_{\mathrm{a}} \tag{3}$$

$$\hat{\mathbf{e}} \approx \bar{\mathbf{e}} + \mathbf{P}_{\mathrm{ae,e}}\mathbf{b}_{\mathrm{ae}} \tag{4}$$

Simultaneously to building the statistical models, the template meshes were further decimated until the number of vertices was below 200, thus clustering the vertices of each template mesh around sparse points, while still preserving the anatomy. The value of 200 was chosen empirically in order to cover the maximal number of mapping points per anatomy in the dataset (136 for one RV).

Each mapping vertex of the full mesh was then approximated to the nearest vertex of the decimated template mesh. This was performed for all subjects within the same CHD group. The mapping frequency of each vertex on the low-resolution mesh was defined as the sum of mapping vertices on the full-resolution mesh, across all subjects in the anatomy-specific dataset.

2.3 Classification

RUSBoost classification of the vertices on a new instantiated shape was performed in order to define target mapping areas (Alg. 1). This particular boosting algorithm is suitable for classes with imbalanced numbers, i.e. regular vertices *vs.* mapping vertices [13]. The features on which the classifier is trained are the concatenated normalised coordinates of all shapes in the database [**x y z**] and their corresponding normalised electrical features [**uni bi LAT**]. The anatomical features in the test set $[\mathbf{x}_{\mathrm{test}}\ \mathbf{y}_{\mathrm{test}}\ \mathbf{z}_{\mathrm{test}}]$ are the normalised Cartesian coordinates of the current shape $\mathbf{s}$, while the unipolar (uni) and bipolar voltages (bi) and the local activation time (LAT) are the normalised electrical features estimated from the SEAM Eq. (4).

2.4 Iterative Addition of Mapping Points

In order to assess the performance of the proposed framework, the computed mapping points were added iteratively to the SEAM in decreasing order of their

Data:
- $(\mathbf{y}_{\text{train}}, [\mathbf{x}_{\text{train}}\ \mathbf{y}_{\text{train}}\ \mathbf{z}_{\text{train}}\ \mathbf{uni}_{\text{train}}\ \mathbf{bi}_{\text{train}}\ \mathbf{LAT}_{\text{train}}])$, $\mathbf{y}_{\text{train}} \in \{0, 1\}$, where 0 denotes regular vertex and 1 mapping vertex.
- number of mapping vertices is significantly lower than the number of regular vertices, i.e. $n_1 \ll n_0$.
- $([\mathbf{x}_{\text{test}}\ \mathbf{y}_{\text{test}}\ \mathbf{z}_{\text{test}}\ \mathbf{uni}_{\text{test}}\ \mathbf{bi}_{\text{test}}\ \mathbf{LAT}_{\text{test}}])$
- weak learner,
  which does not necessarily yield a good initial classification.

Initialisation: $w_{1,i} = \frac{1}{n_{\text{train}}}, i = \overline{1, n_{\text{train}}}$, where $w_{k,i}$ is the weight of sample i in iteration k and n_{train} is the number of samples in the training set;

while *preset number of iterations not reached* **do**

1. subsample from the full set using the weights $w_{k,i}$, $i = \overline{1, n_{\text{train}}}$;
2. feed the subset and the weights to the learner;
3. learner estimates the labels of the training data;
4. update the weights with the classification error;

end

Result: $\mathbf{y}_{\text{test}}$

Algorithm 1: RUSBoost classification algorithm for computing mapping points on a given electroanatomical map. Adapted from [13].

probability. In each iteration, the known shape vector $\mathbf{s}$ was enhanced with the electrical features of the computed mapping vertices. The electrical parameters of the remaining vertices were estimated as in Eq. (3) and (4). The instantiation error was compared to the one obtained from the ground truth mapping points. For each electrophysiology study, the number of iterations was equal to the number of mapping points exported from CARTO. The iterative instantiation is presented comparatively in Alg. 2.

3 Results

3.1 Statistical Models

Tab. 1 shows the first mode of variation of the SEAM for each anatomy. Among the noticeable features, the SEAM is able to describe the variation in the amount of septal activation in RV and the atrial dilatation, a common issue in CHD. Cross-validation on a leave-one-out basis was performed within the dataset of each CHD anatomy. The mean instantiation errors for shape and electrical properties were also computed. The shape instantiation error $\text{err}_{\mathbf{s}}$ was evaluated in terms of mean Cartesian distance between SEAM-computed vertices position and ground truth, while the error for the electrical values was computed as vertex-wise L1-norm between the true and estimated parameters.

Data:
- decimated template mesh and mapping frequency of each vertex, computed according to Sec. 2.2
- descending order of the vertices on the decimated mesh according to mapping frequency (cluster vertices)
- n_P number of CARTO mapping points

Initialisation: perform SEAM according to Eq. (2–4);
for $i \leftarrow 1$ **to** n_P **do**

Proposed framework	**Ground truth**
1. classify vertices on instantiated electroanatomy; 2. select only vertices mapped to the cluster vertex with i-highest probability; 3. perform SEAM as in Eq. (2–4);	1. add mapping vertices corresponding to the next chronological CARTO point; 2. perform SEAM as in Eq. (2–4);

end

Algorithm 2: Iterative addition of mapping points for SEAM with points computed from the proposed framework and points added chronologically from the ground-truth CARTO point list.

The mapping frequency of the vertices on the low-resolution template mesh of each anatomy was computed according to Sec. 2.2 (Tab. 1). The atlas of mapping frequency was also built on a leave-one-out basis, as for SEAM validation. The atlas was further used in ranking potential mapping points in decreasing order of their probability and added iteratively to refine the SEAM instantiation. The resulting colour-coded maps in Tab. 1 indicate the outflow tract in the RV and the interatrial septum as frequent mapping areas.

3.2 Classification

The adapted RUSBoost classifier was cross-validated CHD-specifically by training and testing it on normalised electroanatomical values within the same anatomical group. Overall, the accuracy averaged at 67.91 %, with a true positive rate (sensitivity) of 54.35 %. The high accuracy at low sensitivity in $\mathrm{RA}_{\mathrm{Fontan}}$ indicates that the true negative rate is high, i.e. the model is reluctant to recommend a vertex as a mapping point if not enough previous cases are available.

3.3 Iterative Addition of Mapping Points

Mapping points selected by the classifier and ordered by their mapping frequency according to the anatomy-specific atlas were added iteratively to the SEAM to

	RV	**RA$_{\text{Fallot}}$**	**LA**	**RA$_{\text{Fontan}}$**	**TCPC**
$+2\sigma$	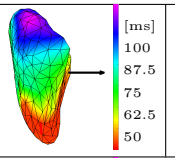	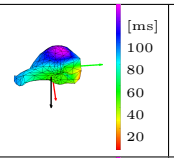	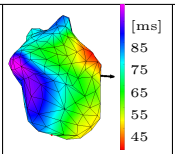	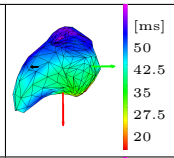	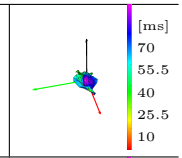
mean	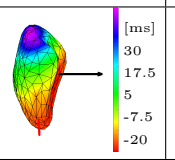	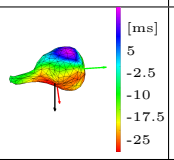	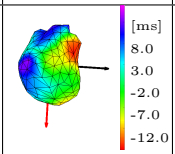	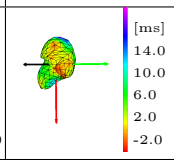	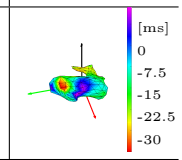
-2σ	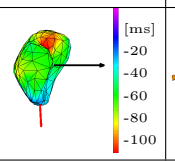	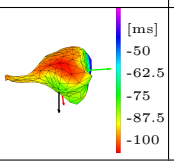	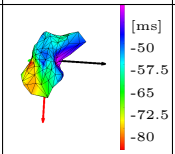	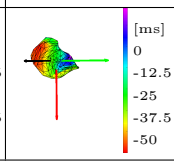	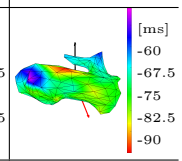
$\text{err}_{\mathbf{s}}$ [mm]	3.69±2.75	3.29±3.17	2.42±2.44	1.96±2.08	5.58±4.63
err_{uni} [mV]	1.51±1.02	0.44±0.23	0.89±1.72	1.11±1.39	1.04±1.73
err_{bi} [mV]	1.22±1.22	0.37±0.21	0.84±1.50	0.74±0.87	1.25±2.60
err_{LAT} [ms]	13.82±18.82	27.31±13.19	22.33±14.30	33.83±13.42	23.63±17.09
map prob	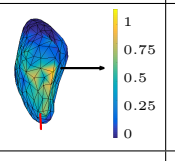	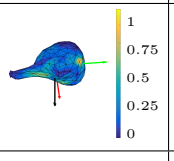	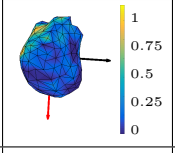	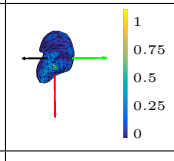	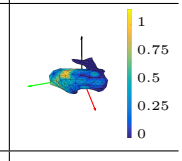
acc [%]	66.61	64.22	66.21	68.64	73.87
sens [%]	71.52	60.32	50.84	36.88	52.22
err_{uni} [mV]		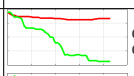	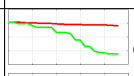	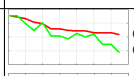	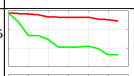
err_{bi} [mV]	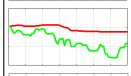	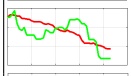	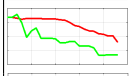	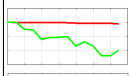	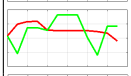
err_{LAT} [ms]	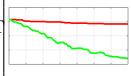	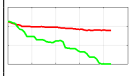	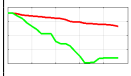		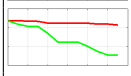
	24 points	70 points	78 points	58 points	33 points

Table 1: SEAM modes of variation and instantiation errors, probabilistic mapping atlas (second set of meshes), accuracy and sensitivity of the RUSBoost classifier and SEAM error reduction with the addition of mapping points computed by the proposed method (green) when compared with the addition of CARTO-exported mapping points (red). The mesh orientation is given by the superior-inferior axis (red), left-right axis (black), and anterior-posterior axis (green).

improve its performance and test the contribution of the proposed mapping points. Starting with no electrical information (original SEAM), the unipolar and bipolar voltages and LATs of vertices in the regional cluster with i-highest mapping probability were added in iteration i. Fig. 1 shows snapshots of the improvement over 3 iterations for a RV. Tab. 1 also includes the curves of error reduction for one case of each CHD anatomy.

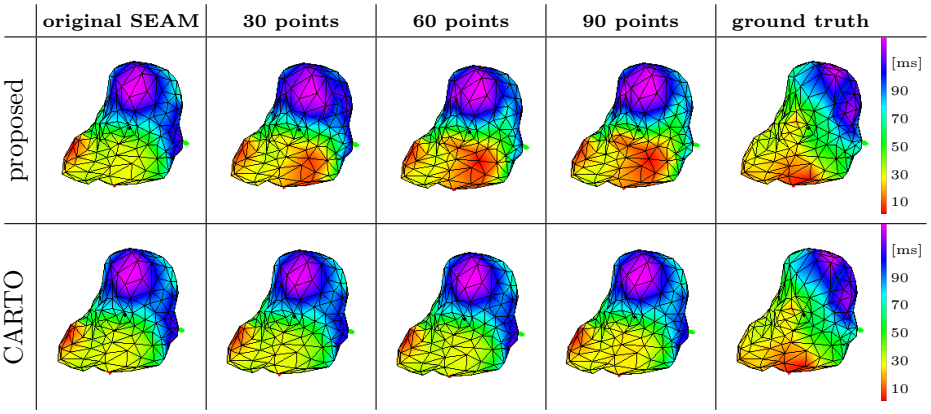

Fig. 1. Iterative addition of mapping points for a RV. Comparison of proposed combined SEAM-classification method with the chronological addition of mapping points as exported from CARTO. The electroanatomical maps show electrical propagation in terms of LAT. The ground truth is the CARTO-exported LAT map.

4 Discussion and Conclusion

Electroanatomical mapping as pre-procedural planning of cardiac catheter ablation is a patient-specific and time consuming step which requires high skills and knowledge from the electrophysiologist. In this paper, a novel combination of statistical electroanatomical mapping model instantiation and classification is employed in order to compute areas of potential interest based on previous cases of similar disease and on patient preoperative anatomical data.

The chain of methods relies on the instantiation of a pure shape model from known anatomy and the direct substitution into a combined SEAM to recover the electrical data. While initial results presented in Tab. 1 are promising, the method relies on the approximation that the shapes in the two models are equal. A quantitative analysis showed that they differ in reality by an average of 3 mm, which is in the range of the shape recovery error of the SEAM. The proposed framework was tested in an iterative addition of the computed mapping points to the SEAM. The error curves in Tab. 1 show good results for a large representative training dataset, e.g. RV (21 cases), but inconclusive results for a database

smaller than 10 subjects (e.g. TCPC). Moreover, a statistical analysis on CHD electroanatomy was only possible due to the electrical activation pattern homogeneity, which needs further investigation in application to other patient groups, such as myocardial infarction survivors.

In conclusion, a novel method for objective identification of electroanatomical mapping areas was proposed. The framework can be regarded as a first step in computer-aided standardisation of pre-procedural mapping in cardiac catheter ablation and can be used to transfer expert knowledge to trainees. Moreover, targeted patient-specific electroanatomical mapping can help in reducing the overall intervention time and to effectively detect potential ablation sites.

References

1. A. Andreopoulos and J. K. Tsotsos. Efficient and generalizable statistical models of shape and appearance for analysis of cardiac MRI. *Med Image Anal*, 12(3):335–57, 2008.
2. Paolo Cignoni, Massimiliano Corsini, and Guido Ranzuglia. Meshlab: an open-source 3D mesh processing system. In *ERCIM News*, pages 45–46.
3. M. A. Constantinescu, S. L. Lee, N. V. Navkar, W. Yu, S. Al-Rawas, J. Abinahed, G. Zheng, J. Keegan, A. Al-Ansari, N. Jomaah, P. Landreau, and G. Z. Yang. Constrained statistical modelling of knee flexion from multi-pose magnetic resonance imaging. *IEEE Trans Med Imaging*, 35(7):1686–95, 2016.
4. K. Roy, F. Gomez-Pulido, and S. Ernst. Remote magnetic navigation for catheter ablation in patients with congenital heart disease: A review. *J Cardiovasc Electrophysiol*, 27 Suppl 1:S45–56, 2016.
5. T. F. Cootes, C. J. Taylor, D. H. Cooper, and J. Graham. Active shape models-their training and application. *Computer Vision and Image Understanding*, 61(1):38–59, 1995.
6. M. M. El Yaman, S. J. Asirvatham, S. Kapa, R. A. Barrett, D. L. Packer, and C. B. Porter. Methods to access the surgically excluded cavotricuspid isthmus for complete ablation of typical atrial flutter in patients with congenital heart defects. *Heart Rhythm*, 6(7):949–56, 2009.
7. M. W. Krueger, G. Seemann, K. Rhode, D. U. Keller, C. Schilling, A. Arujuna, J. Gill, M. D. O'Neill, R. Razavi, and O. Doessel. Personalization of atrial anatomy and electrophysiology as a basis for clinical modeling of radiofrequency ablation of atrial fibrillation. *IEEE Trans Med Imaging*, 32(1):73–84, 2013.
8. T. Mansi, I. Voigt, B. Leonardi, X. Pennec, S. Durrleman, M. Sermesant, H. Delingette, A. M. Taylor, Y. Boudjemline, G. Pongiglione, and N. Ayache. A statistical model for quantification and prediction of cardiac remodelling: application to tetralogy of fallot. *IEEE Trans Med Imaging*, 30(9):1605–16, 2011.
9. D. Perperidis, R. Mohiaddin, and D. Rueckert. Construction of a 4D statistical atlas of the cardiac anatomy and its use in classification. *Med Image Comput Comput Assist Interv*, 8(Pt 2):402–10, 2005.
10. A. Prakosa, M. Sermesant, P. Allain, N. Villain, C. A. Rinaldi, K. Rhode, R. Razavi, H. Delingette, and N. Ayache. Cardiac electrophysiological activation pattern estimation from images using a patient-specific database of synthetic image sequences. *IEEE Trans Biomed Eng*, 61(2):235–45, 2014.

11. A. Rasoulian, R. Rohling, and P. Abolmaesumi. Lumbar spine segmentation using a statistical multi-vertebrae anatomical shape+pose model. *IEEE Trans Med Imaging*, 32(10):1890–900, 2013.
12. D. Rueckert, L. I. Sonoda, C. Hayes, D. L. Hill, M. O. Leach, and D. J. Hawkes. Nonrigid registration using free-form deformations: application to breast MR images. *IEEE Trans Med Imaging*, 18(8):712–21, 1999.
13. C. Seiffert, T. M. Khoshgoftaar, J. Van Hulse, and A. Napolitano. RUSBoost: A hybrid approach to alleviating class imbalance. *IEEE Transactions on Systems, Man, and Cybernetics - Part A: Systems and Humans*, 40(1):185–197, 2010.
14. M. Sermesant, R. Chabiniok, P. Chinchapatnam, T. Mansi, F. Billet, P. Moireau, J. M. Peyrat, K. Wong, J. Relan, K. Rhode, M. Ginks, P. Lambiase, H. Delingette, M. Sorine, C. A. Rinaldi, D. Chapelle, R. Razavi, and N. Ayache. Patient-specific electromechanical models of the heart for the prediction of pacing acute effects in CRT: a preliminary clinical validation. *Med Image Anal*, 16(1):201–15, 2012.
15. M. Wilms, J. Ehrhardt, and H. Handels. A 4D statistical shape model for automated segmentation of lungs with large tumors. *Med Image Comput Comput Assist Interv*, 15(Pt 2):347–54, 2012.
16. O. Zettinig, T. Mansi, B. Georgescu, E. Kayvanpour, F. Sedaghat-Hamedani, A. Amr, J. Haas, H. Steen, B. Meder, H. Katus, N. Navab, A. Kamen, and D. Comaniciu. Fast data-driven calibration of a cardiac electrophysiology model from images and ECG. *Med Image Comput Comput Assist Interv*, 16(Pt 1):1–8, 2013.
17. H. Zhang, A. Wahle, R. K. Johnson, T. D. Scholz, and M. Sonka. 4-D cardiac MR image analysis: left and right ventricular morphology and function. *IEEE Trans Med Imaging*, 29(2):350–64, 2010.